Solar Energy Materials & Solar Cells 118 (2013) 102–108

Contents lists available at ScienceDirect

Solar Energy Materials & Solar Cells

journal homepage: www.elsevier.com/locate/solmat

Ubiquitous carrier harvesting in organic solar cells with embedded indium–tin-oxide nano-electrodes

Min-Hsiang Hsu [a], Po-Han Chen [a], Peichen Yu [a,*], Jen-Hsien Huang [b], Chia-Hua Chang [a], Yu-Chih Cheng [a], Chih-Wei Chu [b]

[a] Department of Photonics and Institute of Electro-Optical Engineering, National Chiao-Tung University, 1001 University Road, Hsinchu 300, Taiwan, ROC
[b] Research Center for Applied Sciences, Academia Sinica, Taipei 11529, Taiwan

ARTICLE INFO

Article history:
Received 5 March 2013
Received in revised form
19 July 2013
Accepted 30 July 2013
Available online 3 September 2013

Keywords:
Indium tin oxide nanorods
Nano-electrodes
Electrochemical deposition
Organic solar cells

ABSTRACT

Bulk heterojunction in organic solar cells allows adequate interfaces for the dissociation of photo-generated excitons. However, the intermixed donor- and acceptor-like materials do not guarantee successful carrier transport and collections. In this work, we demonstrate ubiquitous carrier harvesting characteristics by using embedded indium–tin-oxide nano-electrodes (NEs) with a conformal electro-polymerized coating of a hole conducting layer. Compared to its planar electrode counterpart, this device exhibits internal quantum efficiency insensitive to the distribution of carrier generation, as determined by angle-resolved absorption spectroscopy and photocurrent characteristics. The ubiquitous carrier harvesting characteristics offer a viable solution to organic thin-film devices fabricated on flexible substrates or operated under diffused ambient light.

1. Introduction

Organic solar cells (OSCs) are promising candidates for inexpensive renewable energy sources made possible by solution processes and reel-to-reel production capabilities [1–3]. Assisted by the advent of materials engineering, the performance of OSCs has become very competitive with other thin film materials. For instance, a recently certified device with a record efficiency of over 10.7% has been reported [4], further promoting the applications of OSCs in next-generation photovoltaics. It has been known that the power conversion efficiency (PCE) of an OSC depends on photon absorption, exciton dissociation, and carrier collection, where the first two factors are rarely an issue for polymer–fullerene based solar cells due to highly absorptive active materials and randomly distributed bulk heterojunction (BHJ) structures [5–7]. However, charge transfer still face challenges including unbalanced carrier mobilities, isolated islands, and dead ends formed by donor- and acceptor-like materials [8,9]. To improve carrier collection, recent studies have focused on modifying material properties and processing conditions via surface morphology engineering, solvent annealing, and synthesis methods [10–13]. Novel designs based on nano-materials and nano-fabrication techniques have also been extensively explored [14–19]. Among all, embedded nano-electrodes (NEs) protruded into the active layer have shown the potential to enhance the PCE and to elongate device lifetime, which are both largely attributed to the balanced charge transport [20,21]. Nevertheless, evidence of omni-present carrier collection capability enabled by embedded NEs had not yet been explored. In this work, we demonstrate ubiquitous carrier harvesting characteristics by using embedded indium tin oxide (ITO) NEs. The surface roughness and carrier conduction are retained by applying a conformal electro-polymerization technique of a hole conducting layer (HCL) onto individual nanorods. Compared to the reference cell with a planar electrode (PE), the solar cell with NEs exhibits internal quantum efficiency insensitive to the distribution of carrier generation, determined by angle-resolved absorption spectroscopy and photocurrent characteristics. The omnipresent carrier collection attribute of embedded NEs is very appealing in organic photovoltaic devices with flexible substrates and operated under diffused ambient light.

2. Experimental

The ITO NEs were deposited onto a 1.5 cm × 1.5 cm ITO glass substrate with a thickness of 260 nm and a sheet resistance of 15 Ω/square using oblique electron-beam evaporation at an inclination angle of 70° with respect to the surface normal of the substrate. The target was composed of 5 wt% SnO_2 and 95 wt% In_2O_3. During the deposition, 1 sccm nitrogen gas was introduced under a vacuum pressure of $\sim 10^{-4}$ Torr with a deposition rate of

* Corresponding author. Tel.: +886 (0)35712121 x 56357.
E-mail address: yup@faculty.nctu.edu.tw (P. Yu).

0927-0248/$ - see front matter © 2013 Elsevier B.V. All rights reserved.
http://dx.doi.org/10.1016/j.solmat.2013.07.045

0.15 nm/s at 260 °C for 270 s, growing the rods to around 100–150 nm in height.

The ITO glasses with nano-columns were then treated to an ultrasonic clean process in deionized water, acetone and isopropyl alcohol. The deposition of PEODT was controlled by Autolab potentiostat/galvanostat (Eco Chemie, model PGSTAT30). The 0.01 M monomers EDOT from Aldrich (97%) were dissolved in a 0.1 M $LiClO_4$/acetonitrile solution for a triple-terminal electrochemical process with a platinum foil as the counter electrode, an Ag/Ag^+ reference electrode (0.01 M $AgNO_3$ and 0.1 M $TBAClO_4$ in acetonitrile), and the ITO as the working electrode. The PEDOT films were electro-polymerized onto the ITO nano-columns at 1.1 V versus the Ag/Ag^+ reference electrode with a pre-determined charge density, which controls the thickness of PEDOT film. Then the ITO rods with PEDOT were transferred to a glove box for the subsequent device fabrication process.

The active material was consisted of 2 wt% regioregular P3HT (Mw 3.7×10^4 g mol^{-1}) and 2 wt% PCBM in a dichlorobenzene solution, which were obtained from Rieke Metals and Nano-C Inc., respectively. The solution blend was then spun-cast on to the PEDOT layer at a speed of 600 rpm for 60 s and dried in covered Petri glass dishes for 30 min. Finally, a 30-nm-thick layer of calcium followed by a 60-nm-thick layer of aluminum were thermally coated onto the active material at a pressure of 6×10^{-6} Torr through a 0.1 cm^2 shadow mask. The reference devices with a conventional ITO film electrode were also fabricated with the same processes and conditions.

Efficiency measurements were performed under the simulated AM1.5 G irradiation (100 mW/cm^2) using a Xenon lamp-based Thermal Oriel 1000 W solar simulator and the angular characteristic analyses were carried out via the rotating stage to acquire the data under different incident angles. The spectrum of the solar simulator was calibrated with a PV-measurement (PVM-154) mono-Si solar cell (NREL calibrated), and a Si photo diode with KG-5 color filter (Hamamatsu, Inc.) was used to check the irradiation of the exposed area (100 mW/cm^2). The PVM-154 combined with a KG-5 filter (350–700 nm passed, Newport) was used to simulate a reference solar cell with a spectral response from 350 nm to 700 nm, where the calibration was based on the IEC-69094-1 spectrum [22]. The current density–voltage (J–V) curves were measured with a semiconductor source measure unit (Keithley 2400) using a four-wire connection and the measurements were corrected via the external series resistance. Stability in time was continuously monitored by routinely repeating the measurements on c-Si solar cells. The temperature of the cells was actively controlled during the measurement at 25 ± 1 °C.

The external quantum efficiency (EQE) system is equipped with a 450 W Xenon lamp (Oriel Instrument, model 6266) light source, a water-based IR filter (Oriel Instrument, model 6123 NS) and a monochromator (Oriel Instrument, model 74,100). The beam spot on the sample is rectangular, measuring roughly 1 mm × 3 mm. A calibrated silicon photodetector (Newport 818-UV) was used to calibrate the EQE system before measurements. A lock-in amplifier (Standard Research System, SR830) and an optical chopper controller (SR540), set in voltage mode, were also equipped to lock the output signal and the photocurrent was converted to voltage using a 1-Ω resistor, which was parallel to the sample. The temperature of cells was again actively controlled at 25 ± 1 °C during the measurement.

The angle-resolved absorption measurement system is custom built, which utilizes a 15 cm-radius integrating sphere with a motor-controlled rotational sample stage in the center and a broadband Xenon lamp. The collected reflected photons were then analyzed by a spectrometer (QE65000, Ocean Optics) to obtain the angular reflective spectrum (R) up to an incident angle of 70°. For the sample preparation, because the calcium (Ca) in the devices could be easily oxidized, the layer was removed for the angular-response absorption measurement. The cell absorption (A) can be estimated by subtracting the reflective spectrum by the unity, i.e. $A=1-R$. The system was calibrated by the reflective spectrum of a NIST-standard, intrinsic Si at normal incidence.

3. Results and discussion

The solar cells presented in this work incorporate distributed ITO nanorods which are vertically protruded into the active layers as three-dimensional (3D) electrodes. The highly conductive nanorods allow multiple pathways for low-mobility holes by rendering shortened routes to reach the anode. In other words, the time it took for holes to arrive at the anode is reduced, prompting an increase in the effective hole mobility with respect to the film electrode. Previously, we have observed balanced charge transport achieved with this highly scaffolded cell architecture [21]. The growth of ITO nanorods has been intensively studied over the past few years using various techniques [23]. Herein, we employ an oblique electron-beam deposition technique to place ITO nanorods on a 260-nm-thick ITO-coated glass substrate in an oxygen deficient ambient environment[20,21]. The rod formation involves a self-catalytic vapor-liquid-solid (VLS) process, assisted by introduced nitrogen and high temperature in a vacuum [24]. The incident vapor is set at an angle of 70° with respect to the substrate to control the flux density of molecules on the surface, which facilitates the separation and formation of nuclei. Moreover, the oxygen deficiency allows the segregation of tin-doped indium to form a liquid surface that promotes the absorption of incident vapors, resulting in vertical column growth. Since the nanorods may have different stoichiometric compositions compared to the conventional ITO glass substrate, we also perform an ultraviolet photoelectron spectroscopy (UPS) measurement to determine the work function of ITO nanorods from three samples and use the ITO glass substrate as reference. Preliminary results have shown that the average work function of ITO nanorods is ~4.72 eV, which is slightly lower than that of the reference counterpart at ~4.95 eV. The modification of work function is favored to hole transport, which may contribute to charge collection. Next, to function properly as embedded NEs for organic solar cells, a conformal coating of a HCL around nanostructures is essential in order to maintain the morphology that provides sufficient contact area while effectively blocking electrons. Therefore, an electrochemical deposition of poly-(3,4-thylenedioxythiophene) (PEDOT) was employed via a triple-terminal electrochemical cell. Since the nanorods are highly conductive, EDOT monomers can be gradually polymerized and deposited in the conductive area and therefore, wrap around individual nanorods. Subsequently, the cell fabrication follows the conventional spin-cast of active materials and is capped with calcium and aluminum as the cathode by thermal evaporation. Fig. 1a provides a clear cross-sectional image of a fabricated device, where the active layer is partially released from the substrate. In the dashed red frame, we observe that randomly-oriented nanorod electrodes freely stood on the ITO-coated glass substrate. The orientation and surface morphology was not affected by the device fabrication process or by peeling-off, indicating robust mechanical properties. Fig. 1b shows the distribution of deposited nanorods without the ECD process, where the heights range from 100 to 150 nm with a density of 5×10^9–1×10^{10} cm^{-2}. Next, the deposition of a PEDOT HCL is performed at a charge quantity setting of 50 μC under an applied voltage of 1.1 V based on the optimized conditions described in the previous work [21]. With a lower setting, the coverage of HCL onto the rods is not complete, resulting in shunt losses that lower the fill factor and open circuit voltage. Conversely, at higher settings

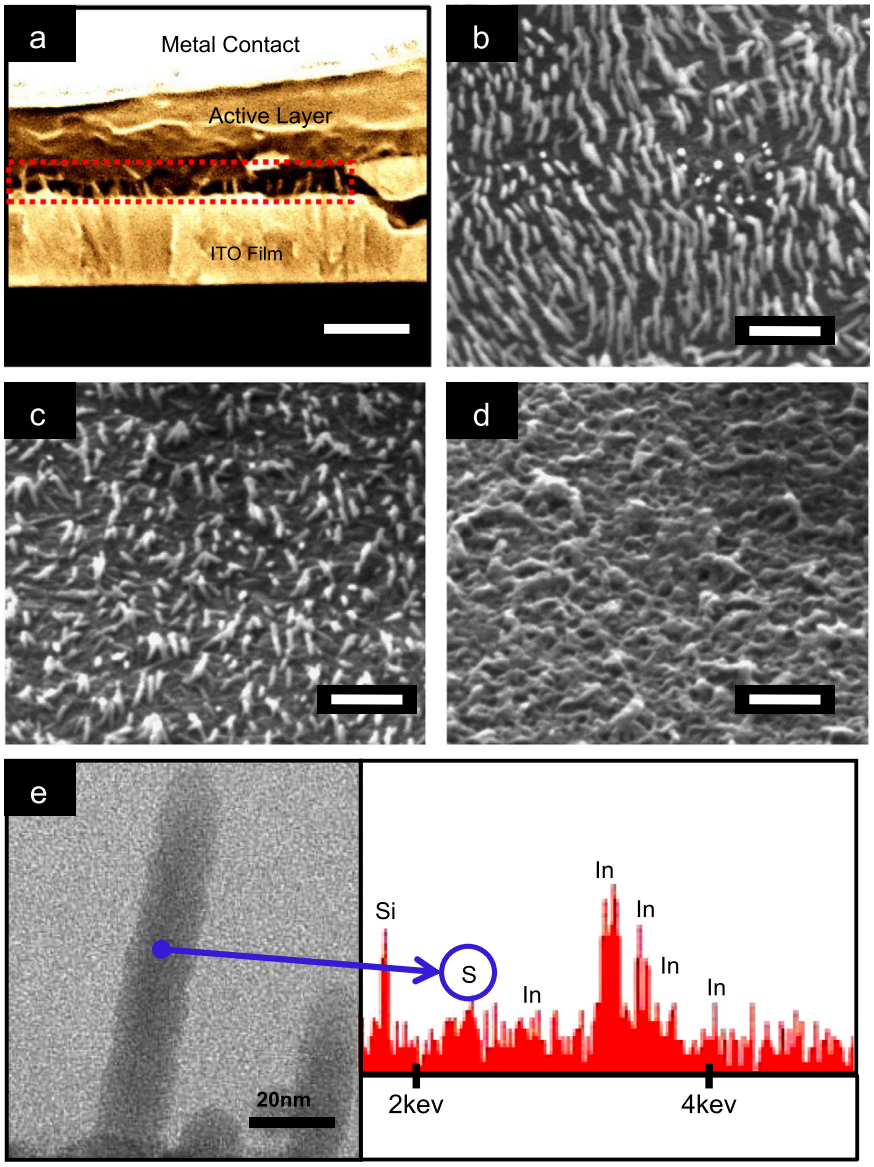

Fig. 1. (a) The cross-sectional image of a fabricated solar cell with embedded NEs, where the active layer is partially released from the substrate. The labeled region indicates that the free-standing NEs are protruded into the active materials, offering mutiple pathways for hole conduction. (b) Indium tin oxide nanorods deposited by oblique electron-beam evaporation. (c) The nanorods coated with a PEDOT hole conducting layer via electro-chemical deposition at an optimized charge quantity of 50 μC under 1.1 V. (d) The reference ITO planar electrode covered with electrochemically deposited PEDOT at an optimized charge setting of 500 μC. The scale bars are 200 nm. (e) Electron dispersive spectroscopic analysis of a single nanorod indicates the exisitence of sulfur, confirming the successful coating of PEDOT on to the side wall.

the large deposition rate at the tips of nanorods, where the electric field is strongest, leads to a cross-linked PEDOT network which planarizes the surface and lowers the output photocurrent. Fig. 1c shows the morphology of nanorods after the optimized ECD process, where the rods become slightly thicker with the PEDOT coating than the bare rods shown Fig. 1b. It can be seen that the spacing between the NEs is still on the order of a few tens to over a hundred nanometers, which is sufficient for the penetration of active materials without altering the organization of BHJ [25]. The X-ray diffraction analysis also shows no significant differences on the P3HT crystallinity for samples with nano-electrodes and with a reference planar electrode (See Supporting Fig. S1). The reference cell is chosen to be a conventional ITO film electrode with an optimized, 30 nm-thick PEDOT layer which is electro-chemically deposited onto the substrate at 500 μC, as shown in Fig. 1d. The PEDOT layer reveals a relatively dense porous structure, which has in the past been shown to enhance the cell performance [26]. Furthermore, an electron dispersive spectroscopic (EDS) analysis is conducted to verify the coating of PEDOT onto the ITO nanorods. As the indicated in Fig. 1e, the spectrum reveals the existence of sulfur, which is one of the characteristic elements of PEDOT, indicating the successful coating of the HCL via the ECD process. However, we note that due to the large beam probe size of an EDS in the micrometer range, it is difficult to resolve the coverage of PEDOT onto the side walls of individual nanorods using this method. In such cases, solar cell characteristics could be employed to reflect the quality of the HCL coating as discussed previously in [21].

The fabricated solar cells with a PE and with NEs were characterized with an angle-resolved reflectance spectroscopy to determine the absorption characteristics ($A=1-R$) modified by the nanorods, as plotted in Fig. 2a and b, respectively. As there have been several technical reports regarding the enhanced optical absorption using surface texturing techniques on either the front or back side of the cell, we note that the height and density of the present nanorods are still not adequate for an evident

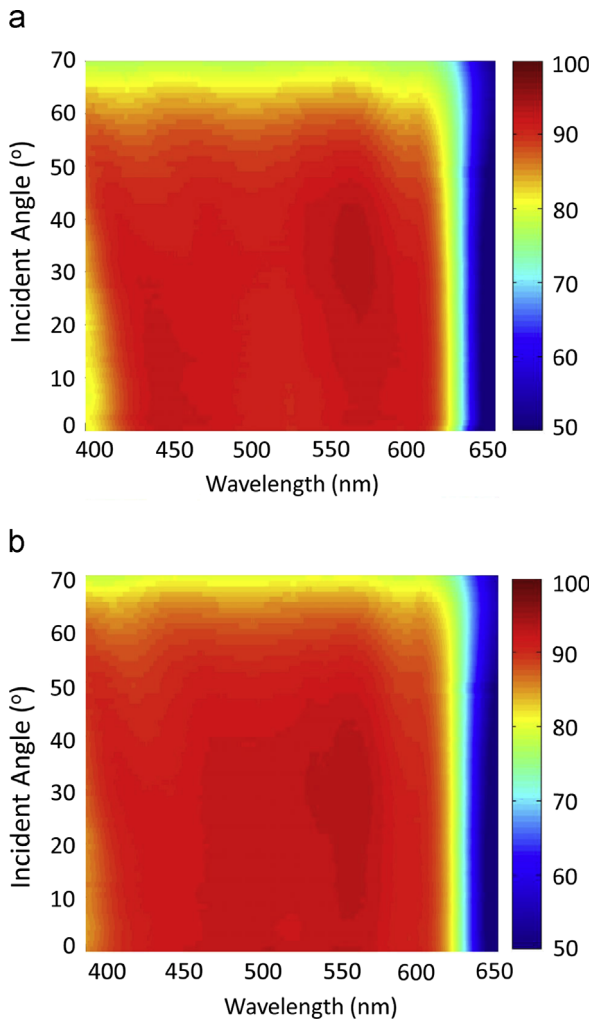

Fig. 2. The measured angular absorption spectra of the (a) PE device and (b) NE device.

antireflection effect, as the AM1.5 G solar-spectrum-weighted absorption is nearly identical across the angles of irradiance incidence from 0° to 70° (see supporting Fig. S2). Nevertheless, we note that the proposed ITO nanostructures for enhanced carrier collection are also compatible with other advanced light harvesting schemes. Although not particularly significant, the modifications of absorption in terms of spectrum and angles of irradiance incidence still need to be taken into account for later device characteristic analyses.

Fig. 3a plots the current density–voltage curves under dark and illuminated conditions for solar cells with a PE and with NEs. The corresponding photovoltaic characteristics are summarized in Table 1, including J_{sc}, open-circuit voltage (V_{oc}), fill factor (FF), and PCE. In general, the cell with NEs exhibits a nearly 10% improvement in J_{sc} and 15% in PCE, which may be ascribed to the increased probability of hole collection resulting from both the modified work function and shortened transport routes via embedded NEs. Previously, we demonstrated that the ratio of carrier mobility with NEs is nearly unity at this optimized ECD setting of 50 μC, where the J_{sc} and PCE is also highest, by making electron- and hole-only devices. However, there had been little evidence as to omnipresent carrier collection capability in a functional device with embedded NEs. The enhancement in J_{sc} or PCE could be attributed to either or both improved optical absorption and carrier collection. Therefore, we first follow the standard procedures to analyze the measured external quantum efficiency (EQE) and absorption (A) to obtain the extracted internal quantum efficiency (IQE), using IQE = EQE/A, as plotted in Fig. 3b, c, and d, respectively. It can be seen that the EQE spectrum indicates a broadband enhancement with the incorporation of NEs, while the absorption merely shows differences of 2–3% in the spectral ranges below 450 nm and between 480 and 560 nm. Consequently, the enhancement in J_{sc} is mostly due to improved carrier collection across the broad absorption range of the photoactive materials, as shown in the IQE spectrum in Fig. 3d. Moreover, previous studies have indicated that parasitic absorptions in the ITO substrate and metals may lead to incorrect IQE analyses which need to be addressed for these devices. We have adopted the methodology proposed by Burkhard et al. to recalibrate the IQE and present the analysis in the supporting information [27]. Because the parasitic absorptions that occur in the PE and NE devices are nearly identical; the broadband IQE enhancement still holds after the calibration. A more detailed description can be founded in the supporting information.

To further investigate carrier collection characteristics, an angular J–V measurement was conducted by mounting the device on a rotatable chuck, and the results are shown in Fig. 4. The calibrated angular photocurrent, $J_{sc}(\theta)$ of both devices decays with the incident angle because the normal component of the irradiance is determined by the cosine of the oblique incidence. In fact, if the measured $J_{sc}(\theta)$ is normalized with the corresponding value at the normal incidence, i.e. $J_{sc}(0)$ for both devices, the angular photocurrent of the cell with NEs exactly follows the cosine curve, while that of the planar counterpart decays faster than the cosine. Still, the difference in decaying trend could arise from either or both optical and electrical transport effects. We then make a further analysis using Eq. (1) by incorporating the measured angle-resolved absorption and IQE spectra.

$$J_{sc}(\theta) = \frac{e}{hc}\int_{400\ \mathrm{nm}}^{650\ \mathrm{nm}} IQE(\lambda,\theta)\, A(\lambda,\theta)\, I_{AM1.5}(\lambda)\, \cos(\theta) d\lambda \quad (1)$$

where IQE(λ,θ) denotes the internal quantum efficiency and A(λ,θ) the absorption, both as functions of the wavelength, λ and the angle of irradience incidence, θ; e is the electric charge, h is Plank's constant, and c is the speed of light. Since A(λ,θ) is experimentally determined as shown in Fig. 2 and only IQE(λ,0) is available as depicted in Fig. 3d, we plot the calculated $J_{sc}(\theta)$ by taking IQE(λ,θ) = IQE(λ,0) as shown in Fig. 4. It can be seen that the measured $J_{sc}(\theta)$ from the cell with NEs matches the calculated values exactly, which confirms the assumption that IQE(λ,θ) = IQE(λ,0). On the other hand, the cell with a PE does not show this characteristic, indicating that the carrier collection capability is dependent on the incident angle of irradience. Since the distribution of carrier generation varies with different angles of irradiance, the angular insensitive IQE characterisitcs indicate that carrier collection capability is spatially invariant to the generation distribution.

Next, we present an electromagnetic simulation to verify the spatial distribution of carrier generation rates, which are derived from optical absorption, at normal and oblique illumination conditions, namely θ = 0°, 45°, and 70°. The corresponding carrier generation distributions, normalized to total generation rates, are presented in color maps overlaid with the profiles of simulated unit cells in Fig. 5a and b for devices with a PE and with NEs, respectively. Here, the incident illumination source is composed of plane waves with an equal component of transverse-electric (TE) and transverse-magnetic (TM) polarizations and weighted with the solar spectrum to represent the broadband and un-polarized sun light. As shown in Fig. 5a, the layered solar cell structure with a PE exhibits a wave-guiding effect to the incident light, where the electromagnetic field distribution resembles a standing wave pattern resulting from multiple reflections at each dielectric interface. At different incident angles, the coupling of solar radiation to the

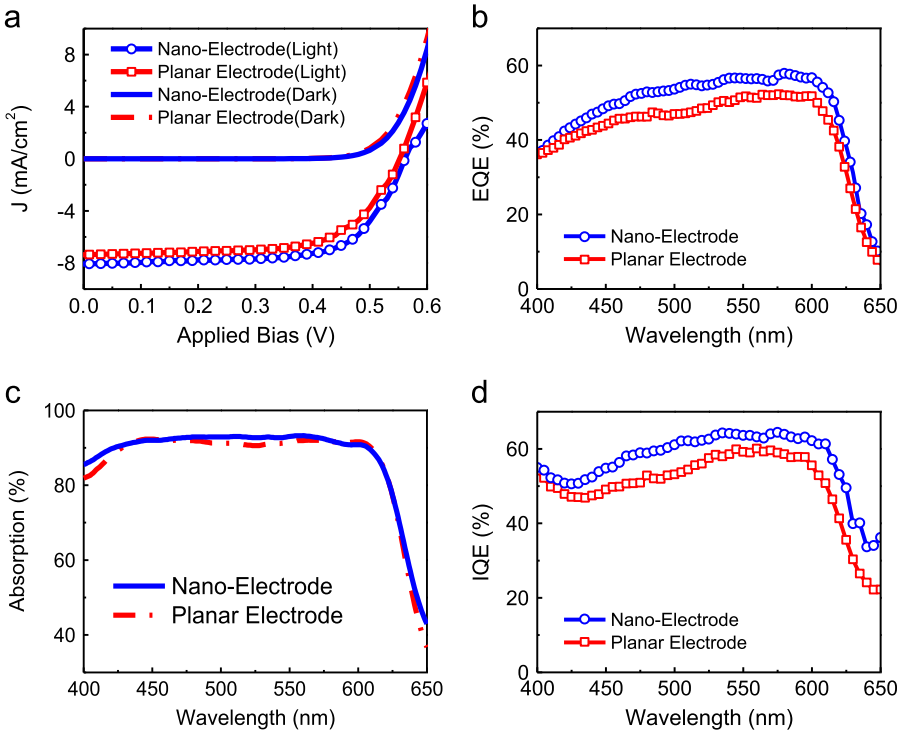

Fig. 3. The measured (a) current density–voltage; (b) external quantum efficiency, EQE and (c) absorption, *A*. (d) The derived internal quantum efficiency, IQE characteristics of solar cells with a PE and NEs using IQE = EQE/*A*.

Table 1
Photovoltaic characteristics of solar cells with a planar electrode and with nano-electrodes.

Device	J_{sc} (mA/cm^2)	V_{oc} (*V*)	FF (%)	PCE (%)
Planar electrode	7.36	0.55	65	2.61
Nano-electrode	8.08	0.56	67	3.01

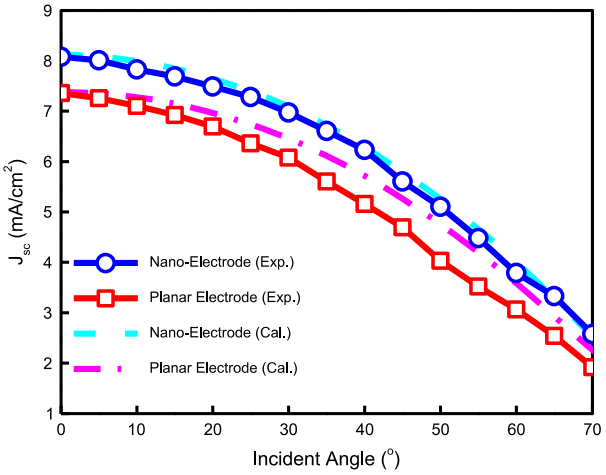

Fig. 4. The measured and calculated photocurrent density (J_{sc}) plotted as a function of the angle of irradiance incidence for cells with a PE and with NEs. The NE device exhibit well matched experimental and calculated values, indicating that the internal quantum efficiency of the cell is insensitive to the illumination incident angle.

solar cell device leads to a spatial shift of absorption peaks, which changes the distribution of carrier generation. The incorporation of nanorods at the interface between the ITO substrate and the active materials reduces the wave-guiding effect, where the contrast of the standing wave pattern is not as strong as with the PE device. However, the spatial occurrences of absorption peaks and dips are still identical due to the sparse distribution of short nanorods which have minimal impact on the dielectric environment to the incident photons. We then average the distributions of the carrier generation rate presented in Fig. 5a and b along the horizontal direction, in order to compare the normalized carrier generation as a function of height, as shown in Fig. 5c–e, for incident angles of 0°, 45°, and 70°. The distributions of carrier generation in the PE and NE devices are similar and indeed vary with the angles of irradiance incidence, which also agree with the observation of angular absorption characterization (see supporting Fig. S2). Since absorption and carrier generation for both devices are nearly identical, we deduce that the carrier collection capability associated with the IQE results in different output photocurrent. Based on our previous analysis, the IQE for the device with a PE shows strong angle dependence, indicating that the carrier collection is indeed affected by distribution of the carrier generation determined by illumination. On the other hand, the device with NEs exhibit angle-independent IQE characteristics, which mitigates the effect of oblique illumination and is an indicator for ubiquitous carrier collection. As solar radiation has more than 30% of diffused components, the omni-present carrier harvesting property uniquely presented in protruded ITO NEs is particularly desirable for organic thin-film devices on flexible substrates and operated under diffused ambient light.

4. Conclusions

In conclusion, we show evidence of a polymer–fullerene based solar cell with embedded indium–tin-oxide nano-electrodes that demonstrate an omni-present carrier collection capability. Compared to a planar-electrode reference, the internal quantum efficiency spectrum with nano-electrodes exhibits broadband enhancements and is insensitive to the angle of irradiance incidence, as well as the distribution of carrier generation. The unique carrier harvesting

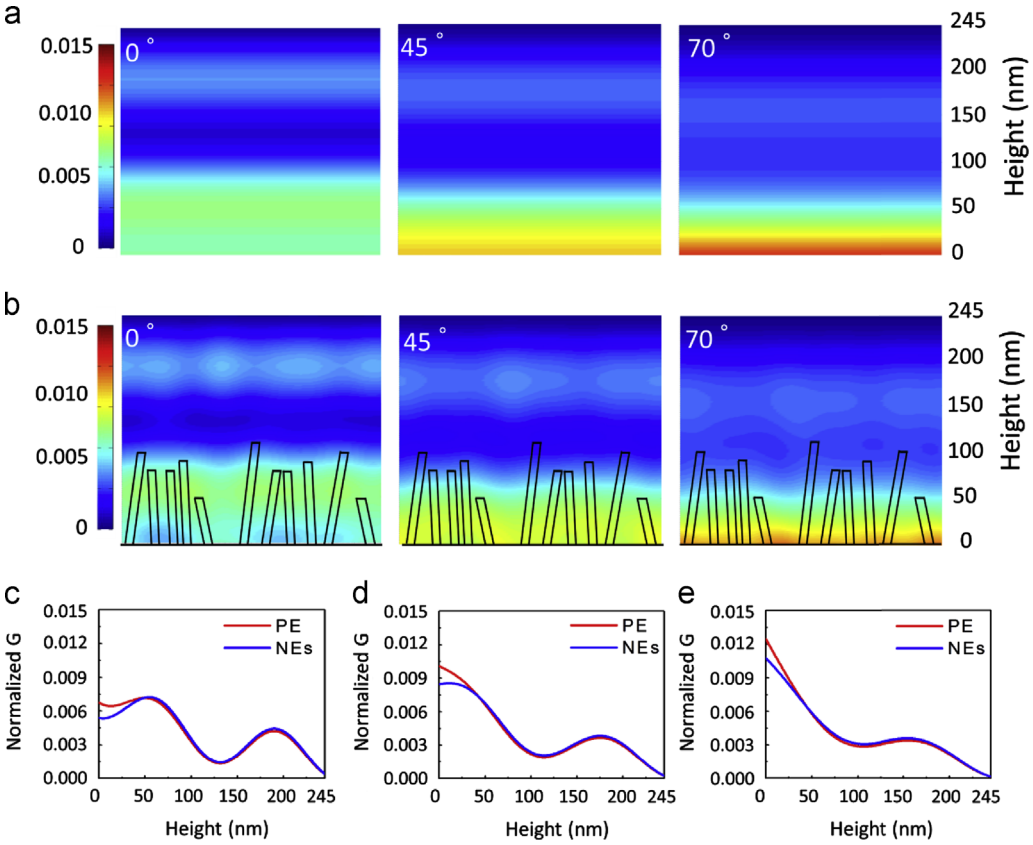

Fig. 5. Mappings of the normalized carrier generation rate (G) for solar cells (a) with a PE and (b) with NEs at illumination incident angles of 0°, 45°, and 70°. Average carrier generation rate as a function of height for illumination incident angles of (c) 0°, (d) 45°, and (e) 70°.

attribute is vital to devices operated under diffused ambient light and also provides an insight into the attainment of high-efficiency organic thin-film photovoltaics with flexible substrates.

Acknowledgment

This work is founded by the National Science Council in Taiwan under Grant no. 100-2628-E-009-020-MY3.

Appendix A. Supplementary material

Supplementary data associated with this article can be found in the online version at http://dx.doi.org/10.1016/j.solmat.2013.07.045.

References

[1] B. Zimmermann, M. Glatthaar, M. Niggemann, M.K. Riede, A. Hinsch, A. Gombert, ITO-free wrap through organic solar cells—A module concept for cost-efficient reel-to-reel production, Solar Energy Materials & Solar Cells 91 (2007) 374–378.
[2] T.D. Nielsen, C. Cruickshank, S. Foged, J. Thorsen, F.C. Krebs, Business, market and intellectual property analysis of polymer solar cells, Solar Energy Materials & Solar Cells 94 (2010) 1553–1571.
[3] F.C. Krebs, T. Tromholt, M. Jorgensen, Upscaling of polymer solar cell fabrication using full roll-to-roll processing, Nanoscale 2 (2010) 873–886.
[4] Heliatek Achieves World Record 10,7% Efficiency, May 2012, ⟨http://www.heliatek.com/⟩.
[5] G. Dennler, M.C. Scharber, C.J. Brabec, Polymer-fullerene bulk-heterojunction solar cells, Advanced Materials 21 (2009) 1323–1338.
[6] S. Gunes, H. Neugebauer, N.S. Sariciftici, Conjugated polymer-based organic solar cells, Chemical Reviews 107 (2007) 1324–1338.
[7] K.M. Coakley, M.D. McGehee, Conjugated polymer photovoltaic cells, Chemistry of Materials 16 (2004) 4533–4542.
[8] S.S.V. Bavel, M. Barenklau, G.D. With, H. Hoppe, J. Loos, P3HT/PCBM bulk heterojunction solar cells: impact of blend composition and 3D morphology on device performance, Advanced Functional Materials 20 (2010) 1458–1463.
[9] J.H. Huang, F.C. Chien, P. Chen, K.C. Ho, C.W. Chu, Monitoring the 3D nanostructures of bulk heterojunction polymer solar cells using confocal lifetime imaging, Analytical Chemistry 82 (2010) 1669–1673.
[10] W. Ma, C. Yang, X. Gong, K. Lee, A.J. Heeger, Thermally stable, efficient polymer solar cells with nanoscale control of the interpenetrating network morphology, Advanced Functional Materials 15 (2005) 1617–1622.
[11] G. Li, V. Shrotriya, J. Huang, Y. Yao, T. Moriarty, K. Emery, Y. Yang, High-efficiency solution processable polymer photovoltaic cells by self-organization of polymer blends, Nature Materials 4 (2005) 864–868.
[12] F. Padinger, R.S. Rittberger, N.S. Sariciftci, Effects of postproduction treatment on plastic solar cells, Advanced Functional Materials 13 (2003) 85–88.
[13] Y. Kim, S. Cook, S.M. Tuladhar, S.A. Choulis, J. Nelson, J.R. Durrant, D.D. C. Bradley, M. Giles, I. McCulloch, C.S. Ha, M. Ree, A strong regioregularity effect in self-organizing conjugated polymer films and high-efficiency polythiophene:fullerene solar cells, Nature Materials 5 (2006) 197–203.
[14] M.S. Kim, J.S. Kim, J.C. Cho, M. Shtein, L.J. Guo, J. Kim, Flexible conjugated polymer photovoltaic cells with controlled heterojunctions fabricated using nanoimprint lithography, Applied Physics Letters 90 (2007) 123113-1–123113-3.
[15] J.T. Chen, C.S. Hsu, Conjugated polymer nanostructures for organic solar cell applications, Polymer Chemistry 2 (2011) 2707–2722.
[16] D.D.S. Fung, L. Qiao, W.C.H. Choy, C. Wang, W.E.I. Sha, F. Xie, S. He, Optical and electrical properties of efficiency enhanced polymer solar cells with Au nanoparticles in a PEDOT–PSS layer, Journal of Materials Chemistry 21 (2011) 16349–16356.
[17] D.A. Rider, R.T. Tucker, B.J. Worfolk, K.M. Krause, A. Lalany, M.J. Brett, J. M. Buriak, K.D. Harris, Indium tin oxide nanopillar electrodes in polymer/fullerene solar cells, Nanotechnology 22 (2011) 085706-1–085706-9.
[18] M.K. Fung, Y.C. Sun, A. Ng, A.M.C. Ng, A.B. Djurišić, H.T. Chan, W.K. Chan, Indium tin oxide nanorod electrodes for polymer photovoltaics, ACS Applied Materials & Interfaces 3 (2011) 522–527.
[19] Z. Hu, J. Zhang, Y. Zhao, Efficient polymer solar cells based on light-trapping transparent electrodes, Applied Physics Letters 100 (2012) 103303-1–103303-4.
[20] P. Yu, C.H. Chang, M.S. Su, M.H. Hsu, K.H. Wei, Embedded indium–tin-oxide nanoelectrodes for efficiency and lifetime enhancement of polymer-based solar cells, Applied Physics Letters 96 (2010) 153307-1–153307-3.

[21] M.H. Hsu, P. Yu, J.H. Huang, C.H. Chang, C.W. Wu, Y.C. Cheng, C.W. Chu, Balanced carrier transport in organic solar cells employing embedded indium–tin-oxide nanoelectrodes, Applied Physics Letters 98 (2011) 073308-1–073308-3.

[22] V. Shrotriya, G. Li, Y. Yao, T. Moriary, K. Emery, Y. Yang, Accurate measurement and characterization of organic solar cells, Advanced Functional Materials 16 (2006) 2016–2023.

[23] M.M. Hawkeye, M.J. Brett, Glancing angle deposition: fabrication, properties and applications of micro- and nanostructured thin films, Journal of Vacuum Science & Technology A 25 (2007) 1317–1335.

[24] Y. Wu, P. Yang, Direct observation of vapor–liquid–solid nanowire growth, Journal of the American Chemical Society 123 (2001) 3165–3166.

[25] S.S.V. Bavel, E. Sourty, G.D. With, J. Loos, Three-dimensional nanoscale organization of bulk heterojunction polymer solar cells, Nano Letters 9 (2009) 507–513.

[26] J.H. Huang, Z.Y. Ho, D. Kekuda, C.W. Chu, K.C. Ho, Controlled growth of nanofiber network hole collection layers with pore structure for polymer–fullerene solar cells, Journal of Physical Chemistry C 112 (2008) 19125–19130.

[27] G.F. Burkhard, E.T. Hoke, M.D. McGehee, Accounting for interface, scattering, and electrode absorption to make accurate internal quantum efficiency measurements in organic and other thin solar cells, Advanced Materials 22 (2010) 3293–3297.